

# Transrectal Ultrasound Image-based Real-time Augmented Reality Guidance in Robot-assisted Laparoscopic Rectal Surgery: A Proof of Concept Study

Jun Shen · Nabil Zemiti · Christophe Taoum · Guillaume Aiche ·  
Jean-Louis Dillenseger · Philippe Rouanet · Philippe Poignet

Received: / Accepted:

**Abstract Purpose** Surgical treatments for low-rectal cancer require careful considerations due to the low location of cancer in rectums. Successful surgical outcomes highly depend on surgeons' ability to determine clear distal margins of rectal tumors. This is a challenge for surgeons in robot-assisted laparoscopic surgery, since tumors are often concealed in rectums and robotic surgical instruments do not provide tactile feedback for tissue diagnosis in real time. This paper presents the development and evaluation of an intraoperative ultrasound-based augmented reality framework for surgical guidance in robot-assisted rectal surgery.

**Methods** Framework implementation consists in calibrating the transrectal ultrasound (TRUS) and the endoscopic camera (hand-eye calibration), generating a virtual model and registering it to the endoscopic image via optical tracking, and displaying the augmented view on a head-mounted display. An experimental validation setup is designed to evaluate the framework.

**Results** The evaluation process yields a mean error of 0.9 mm for the TRUS calibration, a maximum error of 0.51 mm for the hand-eye calibration of endoscopic cameras, and a maximum RMS error of 0.8 mm for the whole framework. In the experiment with a rectum phantom, our framework guides the surgeon to ac-

curately localize the simulated tumor and the distal resection margin.

**Conclusions** This framework is developed with our clinical partner, based on actual clinical conditions. The experimental protocol and the high level of accuracy show the feasibility of seamlessly integrating this framework within the surgical workflow.

**Keywords** Augmented reality · endoscopic camera tracking · surgical gesture guidance · transrectal ultrasound calibration · tumor resection guidance.

## 1 Introduction

Surgery is the main treatment for rectal cancer; surgical outcomes are associated with the quality of life of patients. Specifically, low-rectal cancer is a risk factor for fecal incontinence and requires careful consideration due to its low location in the rectum [1]. Several studies argue that, during distal resection, keeping more tissues in the rectum improves anorectal function [2]. Two surgical procedures, sphincter-preserving resection and ultra-low colorectal anastomosis, meet the requirements of preserving bowel continuity and sphincter function. They consist in: removing part of the rectum including the tumor (i.e., distal resection); then, removing part of the colon (i.e., colon resection); finally, sewing the remaining colon to the remaining rectum (i.e., compression anastomosis). Such interventions are usually performed on patients with supra-anal tumor (tumor's distal end < 60 mm from the anal verge and > 10 mm from the anal ring (Fig. 1) [3]. In conservative surgery, an oncologic rule requires surgeons to perform the distal resection 10 mm below the distal end of the tumor (Fig. 1), and perform the colon resection in the middle of the descending colon, near the inferior mesen-

J. Shen ✉ · J.-L. Dillenseger  
University of Rennes 1, Inserm, LTSI - UMR 1099, F-35000  
Rennes, France.  
E-mail: jun.shen@lirmm.fr

J. Shen · N. Zemiti · C. Taoum · G. Aiche · P. Poignet  
LIRMM, University of Montpellier, CNRS, Montpellier,  
France.

C. Taoum · P. Rouanet  
Institut du Cancer de Montpellier Val d'Aurelle, Montpellier,  
France.

teric artery. For surgeons, performing distal resection is usually the most challenging step, because it is highly dependent upon their experience and ability to determine clear tumor margins. As shown in Fig. 1, the proximal/distal end of the tumor (green) is the proximal/distal margin, and the red line 10 mm below the distal margin is called the distal resection margin.

In robot-assisted laparoscopic surgery, surgeons immediately begin intersphincteric dissection, thereby preventing transanal dissection. Furthermore, robotic instruments facilitate the surgical access to narrow pelvis, and increase the accuracy of surgical gestures. However, it is difficult for surgeons to determine tumor margins during surgery, due to the limited field of view of the endoscopic camera, and the lack of tactile feedback from surgical instruments—which prevents surgeons from diagnosing rectal tissues in real time. In routine practice, a chief surgeon asks an assisted surgeon to show the tumor area by performing digital rectal examination (DRE)—manual palpation in the rectum. But the DRE procedure cannot identify small lesions and does not provide the exact distal resection margin to the chief surgeon; therefore, the distal resection is often performed solely on the basis of the surgeon’s experience. This practice may result in compromised resection margins and must thus be improved.

To the best of our knowledge, to date, only one technique has been proposed for surgical navigation in colorectal surgery: In June 2016, a Florida Hospital (Orlando, FL, USA) team demonstrated a preoperative MRI-based navigation system in transanal endoscopic microsurgery [4]. They attached several markers to the patient’s abdomen for the preoperative MRI imaging and the intraoperative tracking. Then, based on these markers, a tracked surgical tool was registered to, and displayed on, the MRI images—the surgical tool’s location on the MRI images guided the surgeon to reach the tumor area. As a result, however, the marker-based registration does not take the intraoperative rectal tissue deformation into account properly. Hence, intraoperative imaging techniques provide an alternate solution: Indeed, intraoperative ultrasonography (US) can adequately track rectal tissue deformation during surgery. Moreover, some studies have proposed preoperative colonoscopic tattooing (*i.e.*, intraluminal injection in tumor area) to mark tumor location as described in [5]. However, this intraluminal tattooing technique is performed only by a gastroenterologist. Neither precise tumor margins nor distal resection margins can be reliably recognized during surgery based on this technique.

Transrectal ultrasonography (TRUS) is commonly used in rectal cancer staging and is considered an accurate methodology [6]. Additionally, US images are able

to show the rectal wall, pelvic floor muscles and anal sphincter [7]. To date, intraoperative US was used successfully to guide rectal tumor resection in 6 patients, but integrating the US image into the surgical scene causes a heavy mental load for the surgeon [8]. Therefore, we propose to use augmented reality (AR) techniques to alleviate this burden.

The main challenge in implementing an AR system in robot-assisted laparoscopic surgery is to find accurate registration of the medical image to the intraoperative endoscopic view. Manual registration is adequate, if anatomical features are recognized in both medical images and intraoperative endoscopic images. For example, the surgeon manually aligned a virtual kidney model to the intraoperative endoscopic view based on the kidney shape [9]. However, anatomical features of the rectum are not available in robot-assisted laparoscopic surgery, and the use of artificial landmarks is disruptive in the surgical workflow. Optical tracking systems demonstrate the high level of accuracy and reliability in clinical practice, such as hepatobiliary surgery [10] and laparoscopic splenectomy [11]. We therefore opted for one such system to track the TRUS probe and the endoscope for the proposed AR framework.

We propose to localize rectal tumors via intraoperative TRUS and display both the tumor edge and the distal resection margin on the endoscopic view via AR technology in robot-assisted laparoscopic rectal surgery. Accordingly, in this paper, we describe the implementation of a TRUS-based AR framework and evaluate its performance. Several steps were studied: (1) Calibrating the TRUS probe, based on a custom-designed calibration phantom using the method proposed in our previous work [12] (“Ultrasound probe motorization and calibration” section); (2) using and evaluating the hand-eye calibration method proposed in [13] for the 3D endoscopic camera (“Endoscopic camera localization” section); (3) integrating the 3D TRUS and the endoscopic camera into the same geometrical framework, and evaluating it with a rigid phantom (“Framework evaluation” section); (4) designing an experimental setup with a rectum phantom to validate the framework (“Experimental validation and results” section). The experimental results show that the implemented framework guides the surgeon to accurately localize the simulated tumor and the distal resection margin.

## 2 Materials and Methods

The proposed framework is presented in the visualization flowchart (blue) in Fig. 2: A motorized TRUS probe provides a 3D US image which is used to generate the virtual model of the tumor area; then, the virtual

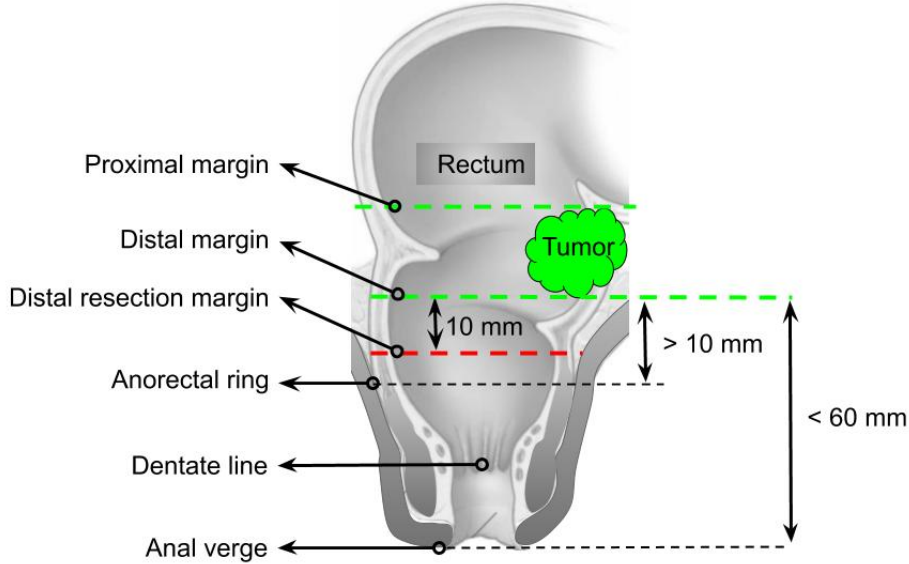


**Fig. 1** Supra-anal tumor in rectum

model is registered to, and superimposed on, the endoscopic view; finally, the augmented view is presented to a user through a head-mounted display (HMD). This HMD device simulates the visualization system of the da Vinci® surgical platform. The accuracy of the AR framework mainly relies on the transformation  ${}^c\mathbf{T}_i$  between the 3D US image  $i$  and the endoscopic view  $c$ . This transformation is computed as shown in the registration flowchart (red) in Fig. 2: Markers  $m1$  and  $m2$  are, respectively, affixed to the endoscope and the TRUS probe for tracking—a tracking system spatially localizes these two markers and provides  ${}^w\mathbf{T}_{m1}$  and  ${}^w\mathbf{T}_{m2}$ . Then, using the transformation  ${}^{m2}\mathbf{T}_i$  (estimated by US calibration in “Ultrasound probe motorization and calibration” section) and  ${}^{m1}\mathbf{T}_c$  (estimated by hand-eye calibration in “Endoscopic camera localization” section), the transformation  ${}^c\mathbf{T}_i$  is computed by:

$${}^c\mathbf{T}_i = ({}^{m1}\mathbf{T}_c)^{-1} ({}^w\mathbf{T}_{m1})^{-1} {}^w\mathbf{T}_{m2} {}^{m2}\mathbf{T}_i \quad (1)$$

where  $i$ ,  $m1$ ,  $m2$ ,  $c$  and  $w$  represent the coordinate systems of the US image, the marker  $m1$ , the marker  $m2$ , the endoscopic camera and the tracking system, respectively.  ${}^b\mathbf{T}_a$  denotes the transformation of coordinate systems  $a$  to  $b$ .

To facilitate the clinical implementation of this AR framework, following materials are used:

- BK Medical Falcon 2101 ultrasound machine and the 8658 TRUS probe
- Atracsys fusionTrack 500 optical tracking system (0.09 mm RMS at up to 2.0 m distance) with passive Navex markers
- ENDOCAM Epic 3DHD endoscopy system (focus-free) from Richard Wolf GmbH
- Sony HMS-3000MT viewing system certified for medical applications

## 2.1 Ultrasound probe motorization and calibration

Reconstructing a 3D US image requires a collection of US frames and their corresponding poses (position and orientation). As shown in Fig. 3, the TRUS probe is driven by a servo motor and rotates along the central axis of the probe; the rotation radius  $r$  (distance from the probe center to the outer rectum wall) is defined as the sum of the rectum wall thickness (it is always smaller than 4 mm [14]) and the probe’s radius (10.5 mm). Assuming proper contact between the rectum and the probe, the rectum wall is always located inside of the rotation radius  $r = 14.5$  mm. We propose a rotation increment of  $\theta = 2.4^\circ$  in order to image the rectum wall with a resolution  $d < 1$  mm (Fig. 3). The motorized TRUS probe provides the range of motion  $170^\circ$ . Moreover, we designed two modes of motorization: In automatic mode, the position of the probe is incremented every 6s, and one ultrasound frame is acquired between two motions; in manual mode, each time a user presses a button, the probe moves  $2.4^\circ$  and produces an US image. For the sake of simplicity, we used k-wave MATLAB toolbox [15] to reconstruct the third dimension of a 3D US image (i.e., scan conversion) by bilinear interpolation. In future experiments, we are aiming to use a 3D built-in TRUS transducer to facilitate the 3D image acquisition.

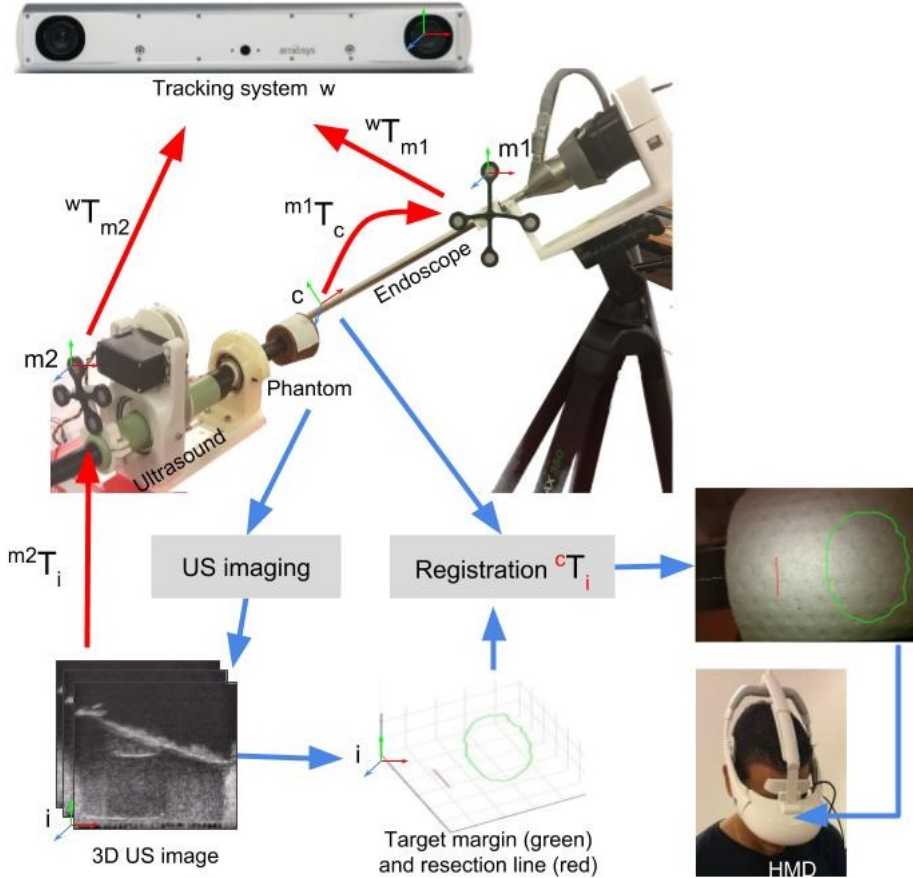


**Fig. 2** Framework overview: blue visualization flowchart and red registration flowchart

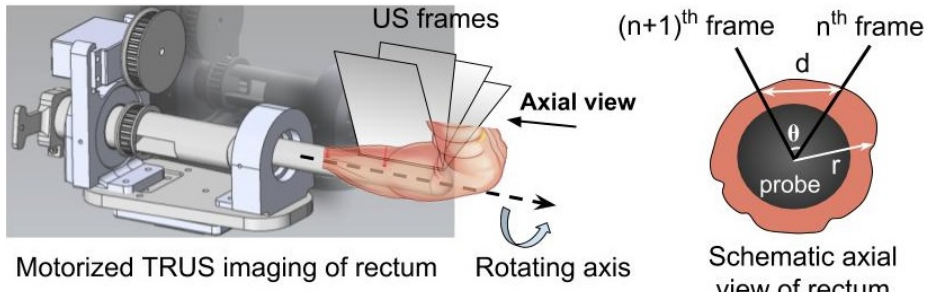


**Fig. 3** TRUS probe motorization and US imaging:  $\theta$ ,  $r$  and  $d$  represent the rotation increment, the rotation radius and the distance between the neighboring US frames, respectively

In Fig. 4, the marker  $m2$  is mounted on the US probe for tracking, and the transformation  $m^2T_i$  between the 3D US image  $i$  and the marker  $m2$  is estimated in the US calibration process. In previous work, we developed a fast and accurate US calibration method based on a 3D-printed phantom—this method streamlines the calibration problem to the registration between the US image and the computer-aided design (CAD) model of the phantom [12]. In order to adapt this method to the motorized TRUS probe, we designed and 3D-printed a specific cylindrical phantom including the precise position of the marker  $m4$  and 4 features: 33 circles with

radii of 2 mm, 3 mm and 4 mm respectively, and one 4 mm  $\times$  15 mm rectangle, as shown in Fig. 4

The calibration procedure started with mounting the cylindrical phantom on the TRUS probe and imaging the phantom in water. In Fig. 4, the phantom's features are extracted from the 3D US image by directional gradients and Standard Hough Transform (SHT) methods [16]; then, using the tracking system and the transformation  $m^4T_i$ —it is estimated by the registration of the extracted features and the phantom's CAD model [12], the calibration solution  $m^2\hat{T}_i$  is found by:

$${}^{m2}\widehat{\mathbf{T}}_i = ({}^w\mathbf{T}_{m2})^{-1} {}^w\mathbf{T}_{m4} {}^{m4}\mathbf{T}_i \quad (2)$$

After the calibration process, the phantom and the marker  $m4$  were removed, but the marker  $m2$  was kept on the US probe for tracking purposes.

The US calibration was evaluated by point reconstruction tests, as presented in [12][17]. In those tests, we measured the distance  $d_{stylus}$  between a point (stylus tip) with a known location in the world coordinate system (WCS) and the same point transformed from the US image to the WCS using the calibration solution  ${}^{m2}\widehat{\mathbf{T}}_i$ . We moved the stylus tip into 5 different positions for point reconstruction tests, and calculated the mean  $\bar{d}_5$  of all the  $d_{stylus}$ :  $\bar{d}_5 = 0.9$  mm. This  $\bar{d}_5$  value includes the error of 3D US image reconstruction which arises from the motorized TRUS probe sweeping over the region of interest. Because rectal tumors can grow through the rectum wall and infiltrate the mesorectal fat 15 mm extension [18], the calibration accuracy was evaluated within the depth of 15 mm.

## 2.2 Endoscopic camera localization

### 2.2.1 Hand-eye calibration

In Fig. 5, marker  $m1$  is mounted on the endoscope for tracking, and the transformation  ${}^{m1}\mathbf{T}_c$  between the endoscopic camera  $c$  and the marker  $m1$  is determined by hand-eye calibration [13]. Prior to using a 3D endoscopic camera, it is necessary to find its intrinsic and extrinsic parameters via Zhang et al. calibration method [19]. Those camera parameters determine the transformation  ${}^c\mathbf{T}_{cb}$  between the chessboard and the endoscopic image in Fig. 5.

We implemented the hand-eye calibration method proposed in Tsai and Lenz [13]. Fig. 5 illustrates the calibration process, in which the endoscopic camera captures the chessboard in  $n$  positions providing  ${}^c\mathbf{T}_{cb}^1$  to  ${}^c\mathbf{T}_{cb}^n$ . Meanwhile, the tracking system tracks the marker  $m1$  giving  ${}^w\mathbf{T}_{m1}^1$  to  ${}^w\mathbf{T}_{m1}^n$ . These measurements are used to compute the  $\mathbf{A}$  and  $\mathbf{B}$  matrices, thereby solving the  $\mathbf{AX}=\mathbf{XB}$  problem.  $\mathbf{X}$  represents the hand-eye calibration solution  ${}^{m1}\widehat{\mathbf{T}}_c$ . In practice, the data acquired in  $n = 17$  different positions are sufficient to estimate an accurate  ${}^{m1}\widehat{\mathbf{T}}_c$ .  $n = 17$  was experimentally chosen, because it gave the best trade-off between the calibration accuracy and the calibration duration.

### 2.2.2 Evaluation

A reflective disk (radius = 5 mm) was used to evaluate the hand-eye calibration solution  ${}^{m1}\widehat{\mathbf{T}}_c$ . In Fig. 6,

${}^{rd}\mathcal{P}$  represents the contour of the reflective disk in its coordinate system  $rd$ . Using  ${}^{m1}\widehat{\mathbf{T}}_c$  and the tracking system—it tracks the disk  $rd$  and the marker  $m1$ ,  ${}^{rd}\mathcal{P}$  is projected to the endoscopic image  $c$  by:

$${}^c\mathcal{P} = ({}^{m1}\widehat{\mathbf{T}}_c)^{-1} ({}^w\mathbf{T}_{m1})^{-1} {}^w\mathbf{T}_{rd} {}^{rd}\mathcal{P} \quad (3)$$

where  ${}^c\mathcal{P}$  represents the virtual information—the green ellipses on the augmented endoscopic images in Fig. 6. As the distance between the green ellipse  ${}^c\mathcal{P}$  and the disk contour is smaller, the transformation  ${}^{m1}\widehat{\mathbf{T}}_c$  is more accurate. This distance is calculated by: (1) extracting the green ellipses and the disk from the augmented endoscopic images using thresholding; (2) in the polar coordinate system centered on the green ellipse, computing the distance  $d_k$  between two pixels—one belongs to the green ellipse and the other one belongs to the disk contour—at the angular coordinate  $\varphi_k = \{0, 5^\circ, 10^\circ, \dots, 355^\circ\}$ ; (3) computing the root mean square  $D_{rms}$  of all the distances  $d_k$ .

The  $D_{rms}$  value varies according to the camera's shooting position and angle. As shown in Fig. 7(a), the endoscopic camera captures the reflective disk in 12 different poses—6 normal poses (poses 1 to 6) and 6 extreme poses (poses 7 to 12). In the extreme poses, the camera is either too close (10 mm in pose 7), too far (90 mm in pose 8) or at an extreme side/high/low angle (poses 9 to 12) relative to the disk. When the camera is positioned in poses 1 to 6,  $D_{rms} < 0.51$  mm (Fig. 7(b)); however, when the camera is placed into extreme poses, the  $D_{rms}$  value increases up to 1.52 mm (Fig. 7(c)). Therefore, in this paper, we used the endoscope in an optimal pose, i.e. 20 mm to 60 mm away from, and  $> 45^\circ$  or perpendicular ( $90^\circ$ ) to the object's surface, as is conventional in rectal cancer surgery (see 'Discussion' section)).

## 2.3 Framework evaluation

To evaluate the implemented framework, we used it to image the cylindrical phantom, and augment the endoscopic view with the US segments of the phantom's features. On the augmented endoscopic images, as shown in Fig. 8, as the green virtual information is closer to the phantom's features, the framework's performance is better. Let  ${}^i\mathcal{S}$  indicate the phantom's features in the US image. Using the US calibration solution  ${}^{m2}\widehat{\mathbf{T}}_i$ , hand-eye calibration solution  ${}^{m1}\widehat{\mathbf{T}}_c$ , and the tracking system—it tracks the marker  $m1$  of the endoscope and the marker  $m2$  of the TRUS probe,  ${}^i\mathcal{S}$  is transformed to the endoscopic camera  $c$  by:

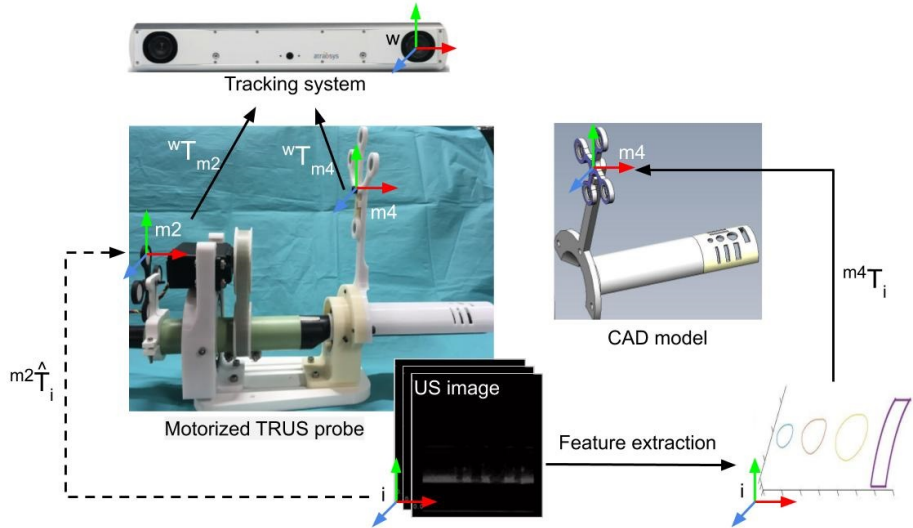


**Fig. 4** US calibration process using a 3D-printed calibration phantom

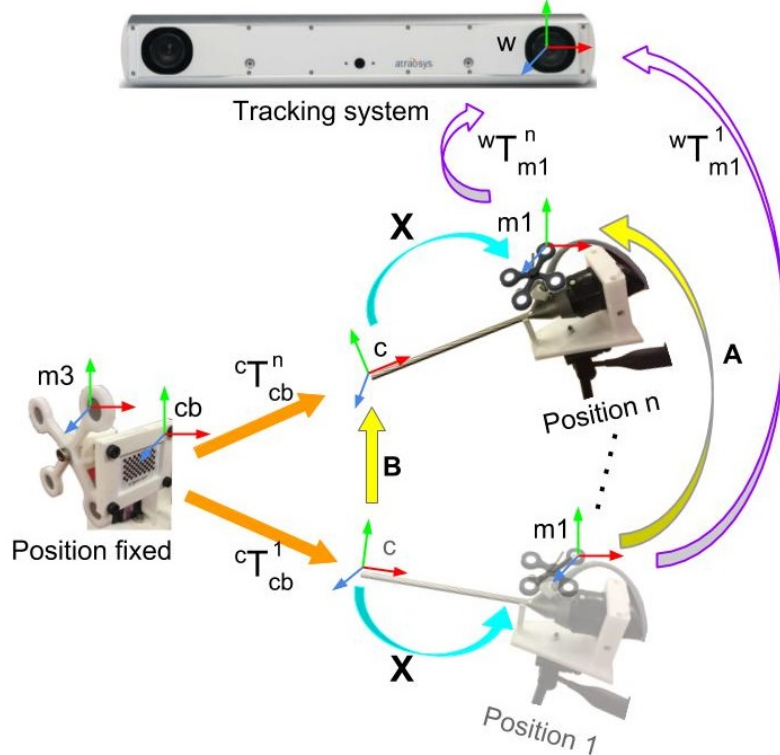


**Fig. 5** hand-eye calibration to estimate transformation  $\mathbf{X}$  ( $m_1 \hat{\mathbf{T}}_c^w$ ) between the endoscopic camera  $c$  and the marker  $m_1$

$${}^c\mathcal{S} = ({}^{m_1}\hat{\mathbf{T}}_c)^{-1} ({}^w\mathbf{T}_{m_1})^{-1} {}^w\mathbf{T}_{m_2} {}^{m_2}\hat{\mathbf{T}}_i {}^i\mathcal{S} \quad (4)$$

${}^c\mathcal{S}$  represents the green virtual model on the endoscopic images in Fig. 8. Then, the distance  $D_{rms}$  between the green virtual model  ${}^c\mathcal{S}$  and the phantom's features (Fig. 8) is computed using the same method in "Evaluation" section (hand-eye calibration evaluation). We obtained  $D_{rms} = 0.45$  mm and  $D_{rms} = 0.8$  mm

for the left and the right views of the 3D endoscopic camera, respectively. The  $D_{rms}$  difference between the left and the right camera views is due to the error from estimating the camera's parameters. However, a framework precision < 1 mm is acceptable in rectal surgery, as confirmed by our clinical partner.

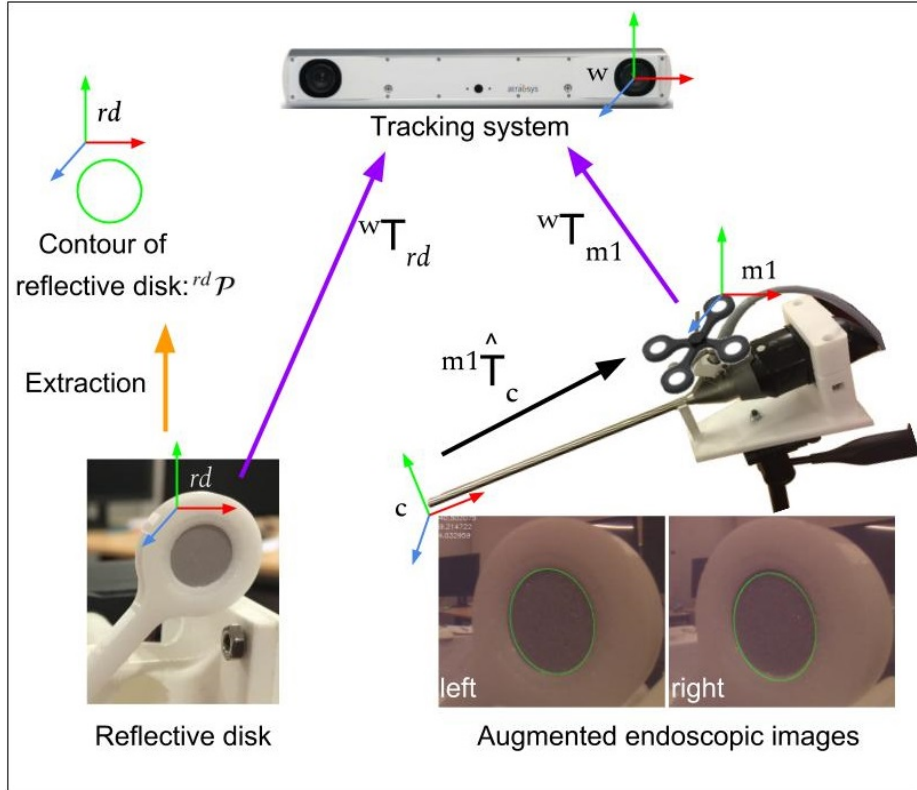


**Fig. 6** Evaluating the hand-eye calibration solution  $m1 \hat{T}_c$  by projecting the reflective disk contour on the endoscopic images

### 3 Experimental Validation and Results

An experimental setup was carried out to validate the implemented framework. During the experiment, a surgeon was guided by the augmented view to remove the simulated tumor from a rectum phantom.

#### 3.1 Experimental validation setup

To integrate the developed framework into robot-assisted laparoscopic rectal surgery, we propose with the clinical partner the following surgical workflow:

- TRUS imaging on rectum after pelvic excision
- Localizing the tumor edge on US images and generating resection margin
- Augmenting the endoscopic view with the tumor edge and resection margin
- Using an electrosurgical device slightly cauterizing the rectal tissues to mark the resection margin
- Withdrawing the US probe from the rectum
- Performing distal resection on the marked area

The experimental setup was designed based on above surgical workflow. As shown in Fig. 9, the framework images a rectum phantom by the TRUS system, and

augments the endoscopic view with the virtual information—it is generated from the 3D US image, as described in Fig. 10. The used rectum phantom was made of silicone, in which a simulated tumor (cylinder-shaped with  $r = 10$  mm and  $h = 10$  mm) was buried. We used a silicone rubber (SMOOTH-ON Ecoflex® 00-50) to simulate the tumor, colored it red and placed it into a rectum-like mold. Then, we filled the mold with another softer type of silicone rubber (SMOOTH-ON Ecoflex® 00-30 colored dark brown) to cover the simulated tumor. These two types of silicone rubbers provide the stiffness difference between the "tumor" and the rest of the "rectum". During the experiment, in order to ensure the simulated tumor was invisible from the surface of the rectum phantom, we covered the phantom surface with a white paper.

In the experiment, a colorectal surgeon wore the HMD for visualization. Based on the augmented view, he used a pen to mark the rectum phantom with the proximal and distal margins of the simulated tumor, and the distal resection margin, as shown in Fig. 11(a). This marking step simulates the electrosurgical device marking rectums with resection margins during surgery. Finally, the surgeon withdrew the TRUS probe and cut the phantom on those marks. The results are analyzed in Fig. 11(b).

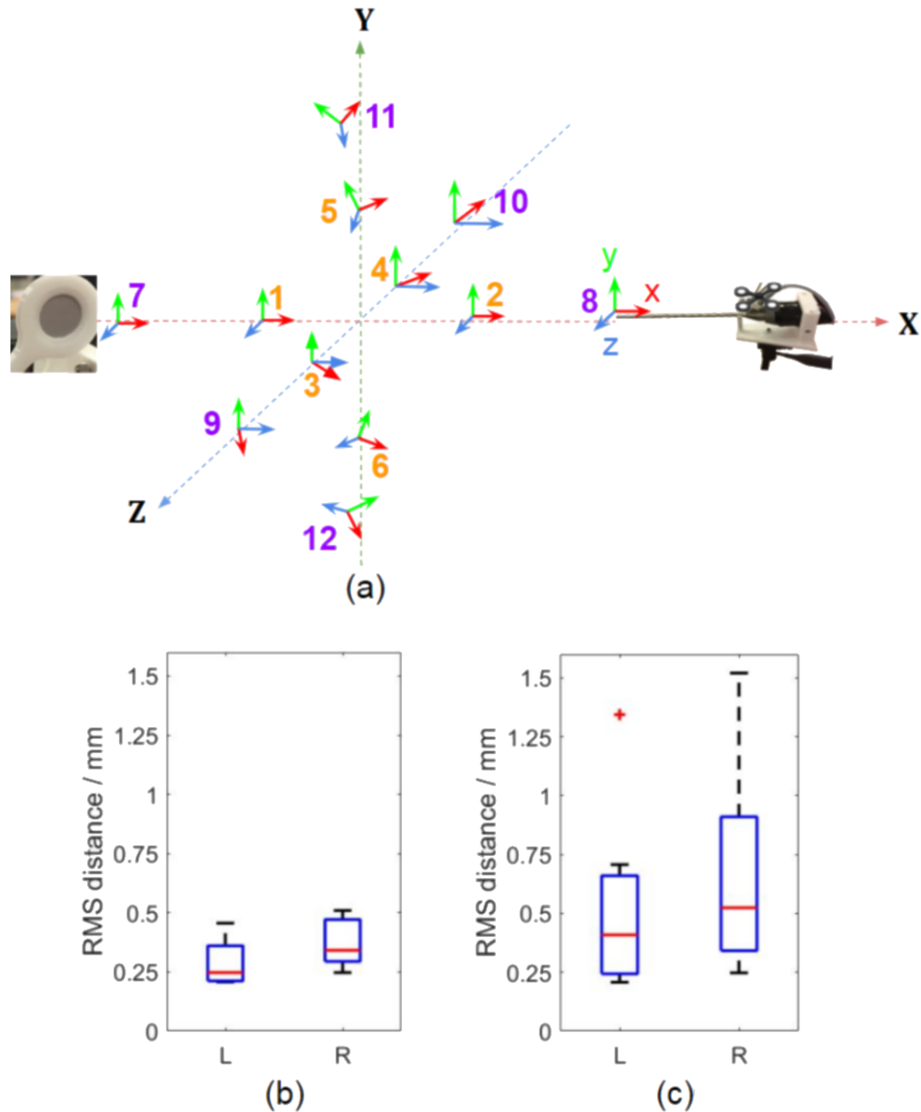


**Fig. 7** (a) Endoscopic camera capturing the reflective disk in 12 poses (normal poses 1 to 6 and extreme poses 7 to 12); boxplot of  $D_{rms}$  values for the left (L) and the right (R) augmented views, when the endoscope operating in normal poses (b) and in both normal and extreme poses (c)

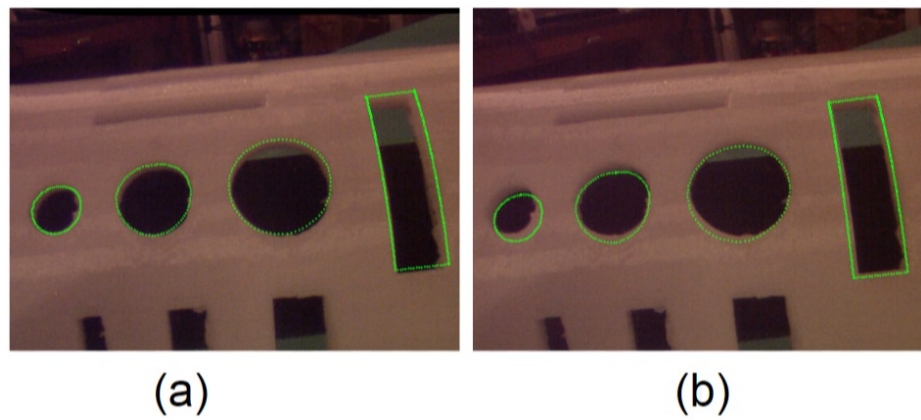


**Fig. 8** Projection of the US segmentation onto the left (a) and the right (b) views of the 3D endoscopic camera

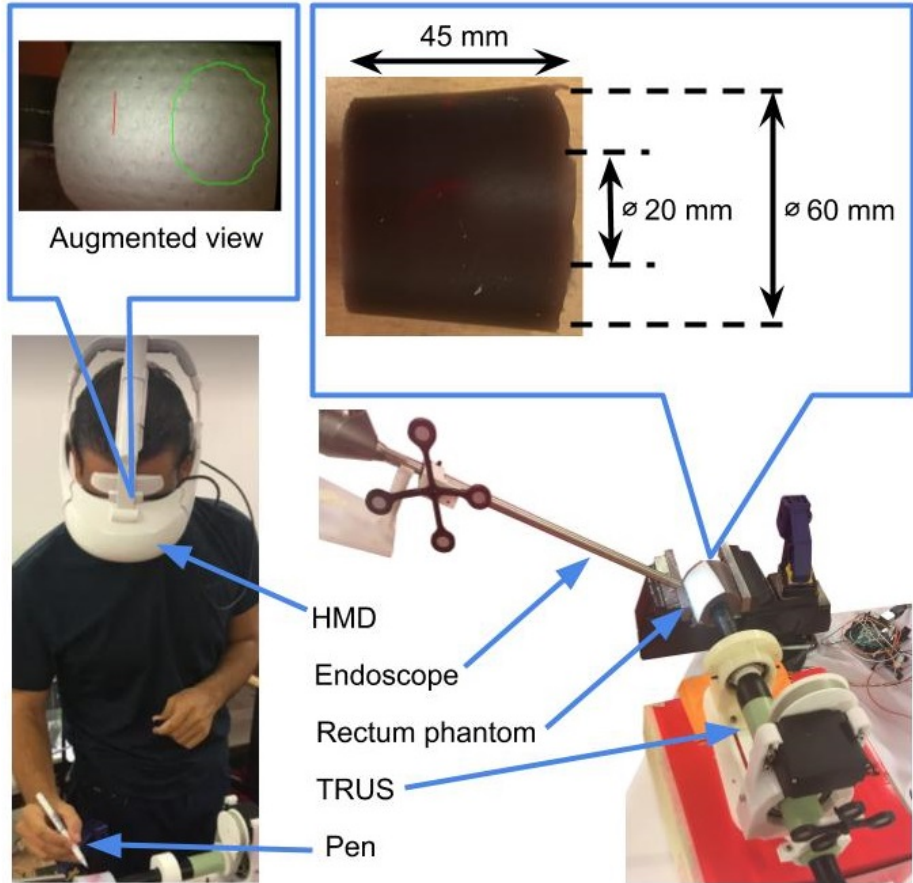


**Fig. 9** Experimental setup: a surgeon marks the rectum phantom based on the augmented endoscopic view

### 3.2 Results

The experimental results are illustrated in Fig. 11. The *mark 1*, *mark 2* and *mark 3* in Fig. 11(a) were made by the surgeon according to the augmented view. Then, the surgeon made straight cuts on these marks through the phantom, and analyzed the cutting surfaces. As shown in Fig. 11(b), on surfaces  $\mathbb{B}$  and  $\mathbb{C}$ , the simulated tumor (red) is clearly seen, however, the red color does not appear on the surface  $\mathbb{A}$  and slightly appears on the surface  $\mathbb{D}$  ( $3 \text{ mm} \times 3 \text{ mm}$  red area). That indicates the *mark 1* and the *mark 2* are on the proximal and distal margins of the simulated tumor, respectively. The distance between *mark 2* and *mark 3* was measured by a ruler giving 10 mm spacing (Fig. 11 (b)). This validates that the *mark 3* is on the distal resection margin. As shown in Fig. 11 (b), the red "tumor" area appears on surface  $\mathbb{D}$  unexpectedly. In order to verify the accuracy of the estimated distal end of the "tumor" (*i.e.* *mark 2*), we resected this "tumor" area into 5 longitudinal slices (approximately 1 mm per slice, as shown in Fig. 12 (a) and (b)). In the worst case, the red "tu-

mor" area appeared at a depth  $< 0.45 \text{ mm}$  in surface  $\mathbb{D}$  (Fig. 12 (c)).

The experimental results show that the implemented framework is able to accurately localize the edge of the simulated tumor, and display the 10 mm distal resection margin to the surgeon, otherwise determined on the basis of the surgeon's experience. Accordingly, this augmented view should facilitate the distal resection step for novice surgeons. This particular point will be evaluated in a dedicated study.

### 4 Discussion

To the best of our knowledge, this is the first proof-of-concept study that estimates the value of intraoperative TRUS imaging and AR technique in the robot-assisted laparoscopic surgery for low-rectal cancer. Indeed, providing real-time AR guidance in laparoscopic rectal surgery is difficult, because of the following reasons: (1) high rectum deformity and elongation during surgery; (2) TRUS probe has to remain operational in the rectum to track the tumor position during surgery, that prevents rectum resection. Our AR framework was

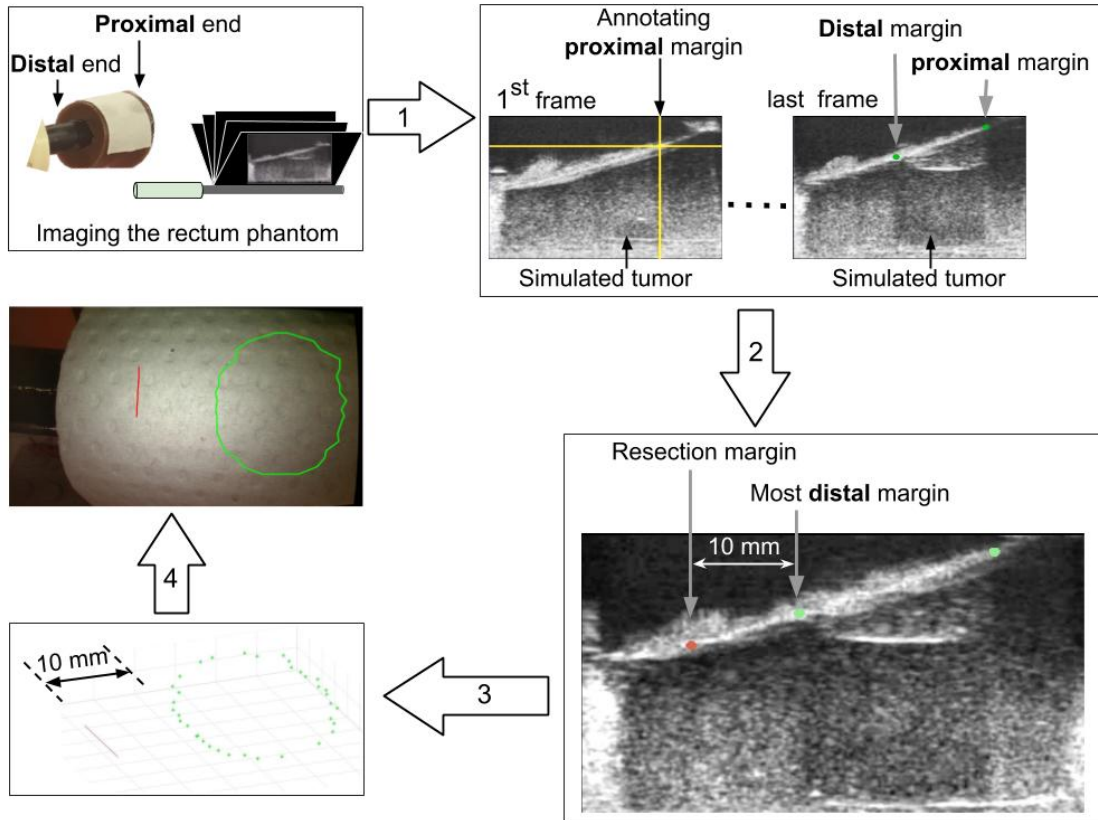


**Fig. 10** Process of generating virtual model from US images: (1) marking the distal and proximal margins (green) of the simulated tumor on US images using crosshairs (yellow); (2) generating the resection margin (red) 10 mm below the most distal margin; (3) collecting all the marks; (4) projecting the marks on the endoscopic view by the transformation  $c\mathbf{T}_i$

designed to solve these issues in AR-guided laparoscopic rectal surgery, as presented in "Experimental validation setup" section.

TRUS compares favorably with other intraoperative imaging modalities (e.g., cone beam computed tomography or open MRI). Indeed, US systems provide real-time imaging; they are less expensive, non-ionizing and easier to integrate in operating rooms. In this work, a fast and accurate phantom-based US calibration method was developed to increase the use of the 3D US imaging technique in operating rooms. Our fully-automated calibration procedure requires no specific skills or user experience. With it, it takes approximately 5 min to calibrate a 3D US probe. Furthermore, this method works on both the motorized TRUS probe and the built-in array 3D US probe, thereby allowing the integration of both types of probes in our framework.

The hand-eye calibration method proposed in [13] insures a high level of accuracy ( $D_{rms} < 0.51$  mm), when the camera is positioned 20 mm to 60 mm from, and  $> 45^\circ$  or perpendicular ( $90^\circ$ ) to the object's surface. The calibration error remains low— $D_{rms} < 1.52$  mm when the endoscopic camera moves into extreme poses—

compared to the distal resection margin (10 mm to the tumor's distal end). We calibrated the endoscopic camera for one zoom/focus setting that corresponds to the practical and approximate distance between the endoscopic camera and the rectum before the step of distal resection (Fig. 13). This is also an optimal pose in which the camera has been calibrated to provide the accuracy  $< 0.51$  mm. The hand-eye calibration for the endoscopic camera takes approximately 10 min during the experiment. However, this step can be executed during patient installation and should not disrupt the surgical workflow. In this work, we used a focus-free 3D endoscope which requires calibration in only one zoom/focus setting. Indeed, da Vinci® platforms use focus-free endoscopes [21]. However, when adjustable-focus endoscopes are used, calibration should be done in multiple zoom/focus settings, as proposed in [22][23].

The implemented framework was first evaluated with the rigid phantom and showed a high accuracy. Moreover, in the experiment with the rectum phantom, the framework guided the surgeon to localize the simulated tumor accurately. For clinical application purposes, we

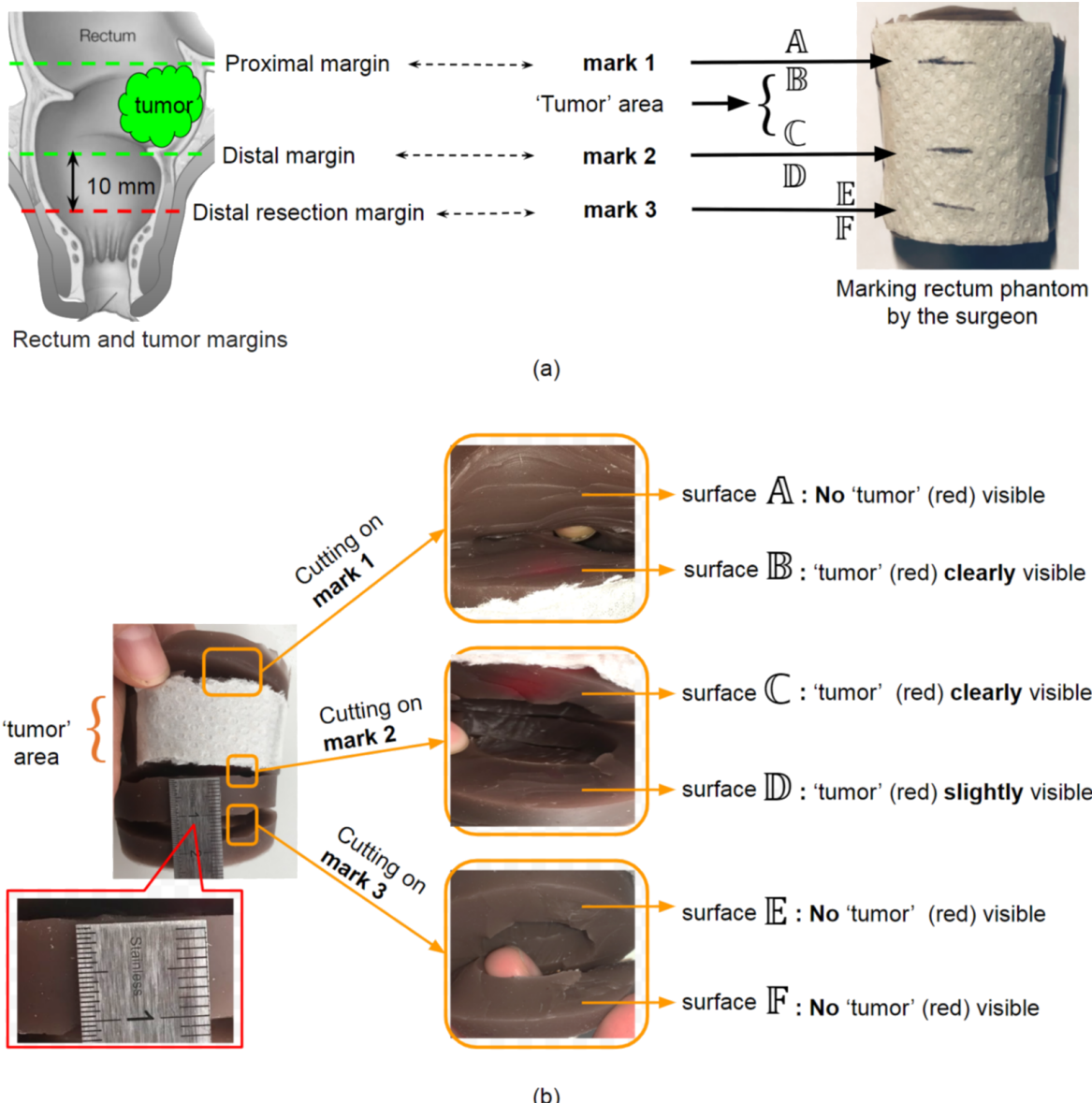


**Fig. 11** Experimental results: (a) the marks (which indicates the proximal/distal margin of the tumor and the distal resection margin) on the rectum phantom; (b) cutting on the *mark 1*, *mark 2* and *mark 3* and analyzing the surfaces

proposed with the clinical partner the following adaptations:

- **Semi-automatic margin generation** In order to find the distal resection margin quickly and precisely, we developed a semi-automatic method: First, a surgeon selects several US frames — the tumor in these US frames is closer to the rectal dentate line (Fig. 1) than it is in other US frames; then, he or she marks the selected US frames with the tumor's distal margin; finally, our algorithm selects the most distal marking — which is the closest one to the dentate line — to generate the resection margin 10 mm below the selected marking. This semi-automatic

method not only improves surgeons' confidence in distal resection by recognizing tumor's distal margin, but also avoids the tedious and time-consuming manual segmentation process. During our experiment, it took the surgeon less than 1 minute to select proper US images and mark them. However, this step must, and will be, evaluated with surgeons to validate the maximum acceptable working time during actual surgery.

- **Marking on rectum** Our framework does tackle the challenge of showing the distal resection margin to surgeons. However, maintaining an accurate augmented view requires the TRUS probe to remain

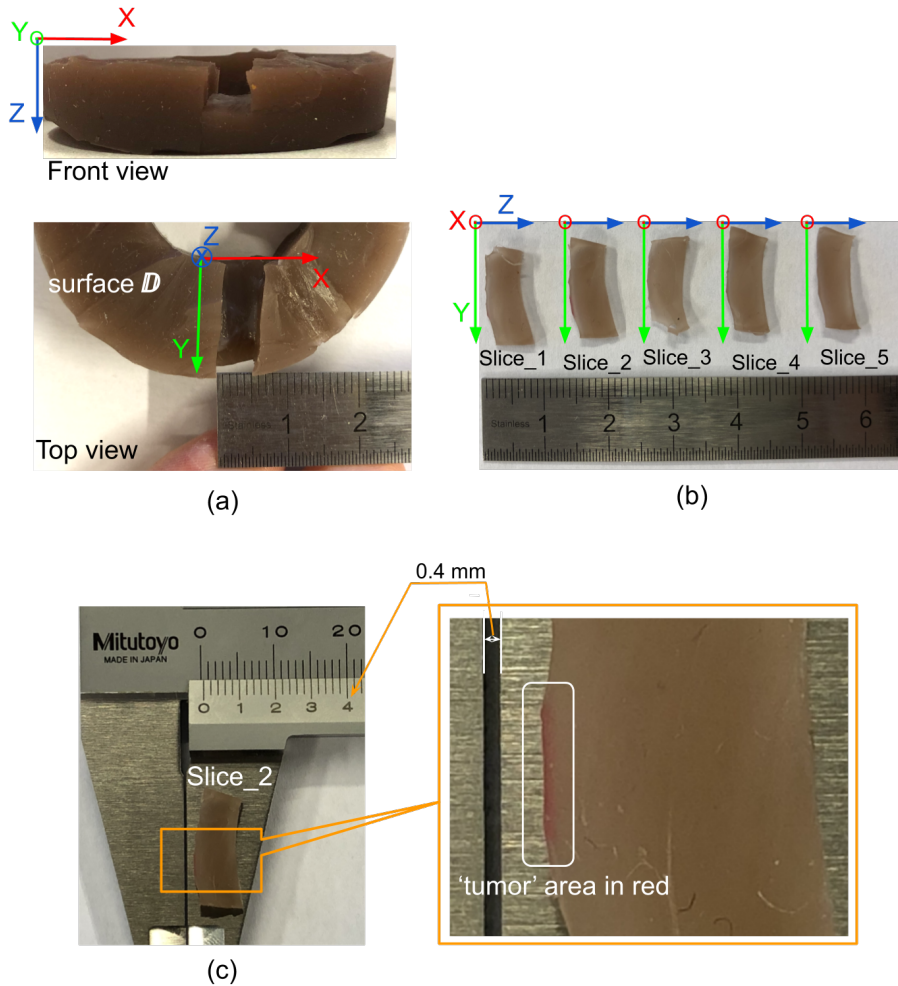


**Fig. 12** Analyzing how deep the 'tumor' infiltrating into surface  $\mathbb{D}$  using a vernier scale

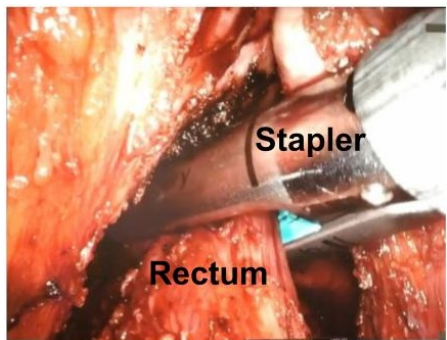


**Fig. 13** Endoscopic view of the distal resection in robot-assisted laparoscopic rectal surgery

operative in the rectum, that prevents the rectal resection. To solve the problem, we propose to keep the probe in the rectum, and use an electro-surgical device to slightly cauterize the rectal tissue on the virtual resection margin. These cauterized marks help surgeons to recognize the resection

margin, after withdrawing the TRUS probe. Such electro-surgical devices are widely accessible in operating rooms. For instance, the da Vinci® surgical platform features a power generator for electro-surgical instruments.

Compared to the preoperative tumor marking technique—colonoscopic tattooing, which provides only tumor location, our method shows to surgeons the precise distal resection margins and does not need a Gastroenterologist in surgery. In literature, some navigation-based solutions have been proposed [4], which do not take into account the intraoperative rectum deformation. To update the navigation platform in real time with tumor location in an elongated rectum, registration of a preoperative image to an intraoperative image, artificial marking of the rectum or biomechanical modeling [20] can be solutions. However, due to the high deformity of rectums during surgery, implementing these methods for navigating rectum resection is very complicated.

In robot-assisted surgery, successful surgical outcomes depend on two main factors: surgical guidance (the purpose of our AR framework), and the surgeon's robotic surgical training. Since the latter is beyond the scope of this paper, in our experiment, the surgeon was asked to perform the rectum phantom resection without a surgical robot. However, to be able to give efficiency metrics of the proposed AR framework (e.g., resection precision, implementation duration and patients medical benefits), a clinical study using our framework needs to be conducted. This is a part of the future work with our clinical partner.

## 5 Conclusion

The main contribution of this work is the efficient implementation of a TRUS-based AR framework. Our overall objective is to apply this process to actual clinical conditions. The framework's performance was evaluated along each implementation step and showed a high level of accuracy. A rectal phantom experiment demonstrated the feasibility of integrating our framework into the surgical workflow. Future work will validate the proposed framework on the *Raven* surgical research platform with an ex-vivo rectum. We will compare the surgical gesture precision of novices and experts, so as to quantify the added value of this framework in terms of improving the surgical learning curve and reducing surgeon mental load.

## Acknowledgments

This work was supported in part by the French National Agency for Research (Agence Nationale pour la Recherche, ANR) within the Investissements d'Avenir Program (Labex CAMI, ANR-11-LABX0004, Labex NUMEV, ANR-10-LABX-20, and the Equipex ROBOTEX, ANR-10-EQPX-44-01) and by the French Region of Brittany.

## Ethical Statements

The authors declare that they have no conflict of interest. This article does not contain any studies with human participants or animals performed by any of the authors. This article does not contain patient data. Informed consent was obtained from all individual participants included in the study.

## References

- Lee TG, Kang SB, Heo SC, Jeong SY, Park KJ (2011) Risk factors for persistent anal incontinence after restorative proctectomy in rectal cancer patients with anal incontinence: prospective cohort study. *World J Surg* 35(8): 1918-1924.
- Lewis WG, Holdsworth PJ, Stephenson BM, Finan PJ, Johnston D (1992) Role of the rectum in the physiological and clinical results of coloanal and colorectal anastomosis after anterior resection for rectal carcinoma. *Br J Surg* 79(10): 1082-1086.
- Rullier E, Denost Q, Vendrely V, Rullier A, Laurent C (2013) Low rectal cancer: classification and standardization of surgery. *Dis Colon Rectum* 56(5): 560-567.
- Atallah S, Larach SW, Monson JR (2016) Stereotactic navigation for TAMIS-TME. *Minim Invasive Ther Allied Technol* 25(5): 271-277.
- Park JW, Sohn DK, Hong CW, Han KS, Choi DH, Chang HJ, Lim SB, Choi HS, Jeong SY (2008) The usefulness of preoperative colonoscopic tattooing using a saline test injection method with prepackaged sterile India ink for localization in laparoscopic colorectal surgery. *Surgical endoscopy* 22(2): 501-505.
- Kav T, Bayraktar Y (2010) How useful is rectal endosonography in the staging of rectal cancer?. *World J Gastroenterol* 16(6): 691-697.
- Beynon J, Foy DM, Temple LN, Channer JL, Virjee J, Mortensen NM (1986) The endosonic appearances of normal colon and rectum. *Dis Colon Rectum* 29(12): 810-813.
- Greif F, Aranovich D, Hananel N, Knizhnik M, Belenky A (2009) Intraoperative ultrasound in colorectal surgery. *J Clin Ultrasound* 37(7): 375-379.
- Su LM, Vagvolgyi BP, Agarwal R, Reiley CE, Taylor RH, Hager GD (2009) Augmented reality during robot-assisted laparoscopic partial nephrectomy: toward real-time 3D-CT to stereoscopic video registration. *Urology* 73(4): 896-900.
- Okamoto T, Onda S, Matsumoto M, Gocho T, Futagawa Y, Fujioka S, Yanaga K, Suzuki N, Hattori A (2013) Utility of augmented reality system in hepatobiliary surgery. *J Hepatobiliary Pancreat Sci* 20(2): 249-253.
- Ieiri S, Uemura M, Konishi K, Souzaki R, Nagao Y, Tsumi N, Akahoshi T, Ohuchida K, Ohdaira T, Tomikawa M, Tanoue K (2012) Augmented reality navigation system for laparoscopic splenectomy in children based on preoperative CT image using optical tracking device. *Pediatr Surg Int* 28(4): 341-346.
- Shen J, Zemiti N, Dillenseger JL, Poignet P (2018) Fast and simple automatic 3D ultrasound probe calibration based on 3D printed phantom and an untracked marker. *Conf Proc IEEE Eng Med Biol Soc* 878-882.
- Tsai RY, Lenz RK (1998) Real time versatile robotics hand-eye calibration using 3D machine vision. *IEEE Int Conf Robot Autom* 554-561.
- Huh CH, Bhutani MS, Farfan EB, Bolch WE (2003) Individual variations in mucosa and total wall thickness in the stomach and rectum assessed via endoscopic ultrasound. *Physiol Meas* 24(4): N15.
- Treeby BE, Cox BT (2010) k-Wave: MATLAB toolbox for the simulation and reconstruction of photoacoustic wave-fields. *J Biomed Opt* 15(2): 021314.
- Duda RO, Hart PE (1972) Use of the Hough transformation to detect lines and curves in pictures. *Commun ACM* 15(1): 11-15.
- Abeysekera JM, Najafi M, Rohling R, Salcudean SE (2014) Calibration for position tracking of swept motor 3-d ultrasound. *Ultrasound Med Biol* 40(6): 1356-1371.

18. Van Loenhout R, Zijta F, Lahaye M, Beets-Tan R, SmithuisR (2015) Rectal Cancer - MR staging 2.0. <https://radiologyassistant.nl/abdomen/rectal-cancer-mr-staging-2-0>
19. Zhang Z (2000) A flexible new technique for camera calibration. *IEEE Trans Pattern Anal Mach Intell* 22: 1330-1334.
20. Payan Y, Ohayon J (2017) Biomechanics of living organs: hyperelastic constitutive laws for finite element modeling. World Bank Publications.
21. Intuitive.com: <https://www.intuitive.com/en-us/products-and-services/da-vinci/vision>
22. Atienza R, Zelinsky A (2001) A practical zoom camera calibration technique: an application on active vision for human-robot interaction. *Australian Conf Robot and Autom*: 85-90
23. Fraser CS, Al-Ajlouni S (2006) Zoom-dependent camera calibration in digital close-range photogrammetry. *Photogramm Eng Remote Sensing* 72(9): 1017-1026.